

# Subspace Alignment for Vision-Language Model Test-time Adaptation

Zhichen Zeng<sup>1</sup>, Wenxuan Bao<sup>1</sup>, Xiao Lin<sup>1</sup>, Ruizhong Qiu<sup>1</sup>, Tianxin Wei<sup>1</sup>, Xuying Ning<sup>1</sup>,  
Yuchen Yan<sup>2</sup>, Chen Luo<sup>2</sup>, Monica Xiao Cheng<sup>2</sup>, Jingrui He<sup>1</sup>, Hanghang Tong<sup>1</sup>

<sup>1</sup>University of Illinois Urbana-Champaign, <sup>2</sup>Amazon,  
 {zhichenz, htong}@illinois.edu

## Abstract

Vision-language models (VLMs), despite their extraordinary zero-shot capabilities, are vulnerable to distribution shifts. Test-time adaptation (TTA) emerges as a predominant strategy to adapt VLMs to unlabeled test data on the fly. However, existing TTA methods heavily rely on zero-shot predictions as pseudo-labels for self-training, which can be unreliable under distribution shifts and misguide adaptation due to two fundamental limitations. First (*Modality Gap*), distribution shifts induce gaps between visual and textual modalities, making cross-modal relations inaccurate. Second (*Visual Nuisance*), visual embeddings encode rich but task-irrelevant noise that often overwhelms task-specific semantics under distribution shifts. To address these limitations, we propose SubTTA, which aligns the semantic subspaces of both modalities to enhance zero-shot predictions to better guide the TTA process. To bridge the modality gap, SubTTA extracts the principal subspaces of both modalities and aligns the visual manifold to the textual semantic anchor by minimizing their chordal distance. To eliminate visual nuisance, SubTTA projects the aligned visual features onto the task-specific textual subspace, which filters out task-irrelevant noise by constraining visual embeddings within the valid semantic span, and standard TTA is further performed on the purified space to refine the decision boundaries. Extensive experiments on various benchmarks and VLM architectures demonstrate the effectiveness of SubTTA, yielding an average improvement of 2.24% over state-of-the-art TTA methods.

## 1 Introduction

Pretrained Vision-Language Models (VLMs), such as CLIP (Radford et al., 2021) and ALIGN (Jia et al., 2021), have demonstrated extraordinary zero-shot capabilities across diverse downstream tasks, ranging from image classification (Radford et al., 2021; Addepalli et al., 2024) to image caption-

ing (Chen et al., 2022; Yu et al., 2022) and visual question-answering (Yu et al., 2023; Huynh et al., 2025). The success stems from the expressive joint embedding space, where visual representations are globally aligned with rich linguistic concepts, enabling task descriptions in natural language to directly retrieve task-relevant visual semantics.

Despite these capabilities, VLMs often struggle when deployed in open-world scenarios which are characterized by distribution shifts, such as image corruptions (Hendrycks and Dietterich, 2019) or stylistic changes (Patashnik et al., 2021). These shifts distort the vision-language embedding space and degrade the reliability of zero-shot predictions. To mitigate this, test-time adaptation (TTA) has emerged as a predominant paradigm to adapt pre-trained VLMs to unlabeled test data on the fly (Osowiechi et al., 2024; Maharana et al., 2025; Bao et al., 2025). Notably, most existing TTA approaches, either training-free methods utilizing memory banks (Zhang et al., 2024; Li et al., 2025a) or training-based methods optimizing pseudo labels (Zhang et al., 2022; Shu et al., 2022), heavily rely on the VLMs’ raw zero-shot predictions to guide the adaptation process, which can be precarious when the aligned space is disrupted. We attribute the failure of standard TTA to two fundamental limitations under distribution shifts, namely *modality gap* and *visual nuisance*.

First (*Modality Gap*), distribution shifts induce a global drift of the visual manifold relative to the textual manifold. Intuitively, as shown in Figure 1a, the modality gap causes visual features (e.g., dog) to drift toward incorrect textual anchors (e.g., bird), leading to incorrect zero-shot predictions. To validate this empirically, we analyze the visual-textual principal angles under different shift levels in Figure 2. We observe that correct predictions consistently exhibit smaller principal angles than mispredictions, and that, as the shift level increases to the right side, the entire distribution

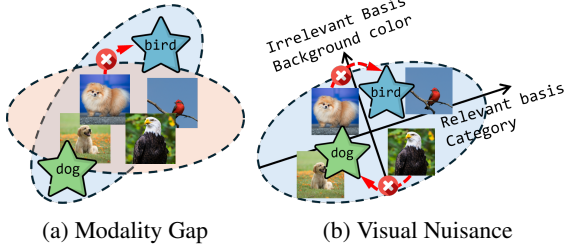


Figure 1: Failure modes of zero-shot prediction. (a) Modality gap: Visual features drift away from the textual manifold. A dog image shifts closer to the bird anchor. (b) Visual Nuisance: Task-irrelevant noise overshadows core semantics. a dog is misclassified as bird due to spurious correlation with the blue sky.

shifts toward larger angles accompanied by a surge in errors. This geometric divergence indicates that the pre-trained vision-language alignment is structurally broken, creating a modality gap where the visual feature space is globally rotated away from the textual anchor space.

Second (*Visual Nuisance*), unlike compact textual anchors, visual embeddings encode rich but task-irrelevant information. As illustrated in Figure 1b, irrelevant nuisances often overshadow core semantics: for example, a dog on a blue background may be misclassified as a bird due to the spurious correlation between the sky color and the bird class. We quantify this phenomenon via semantic concentration, measured by the ratio of visual energy projected onto the textual subspace relative to the raw embedding, in Figure 3. Correct samples exhibit markedly higher semantic concentration than mispredictions, while increasing shift levels push the distributions toward lower concentration, revealing that task-relevant components are increasingly overshadowed by nuisance dimensions. Consequently, pseudo-labels derived from raw visual embeddings are heavily contaminated by irrelevant noise (e.g., background clutter or domain-specific styles), causing TTA to reinforce prediction errors rather than correct them.

To address these challenges, we propose SubTTA, a novel TTA framework grounded in subspace alignment. First (*Geometric Alignment*), to bridge the modality gap, we rectify the global drift of the visual manifold. We construct compact principal subspaces for both modalities via eigendecomposition. Treating the textual basis as an anchor, we geometrically align the visual subspace to it by minimizing the chordal distance. This step recalibrates the visual feature space to match the pre-

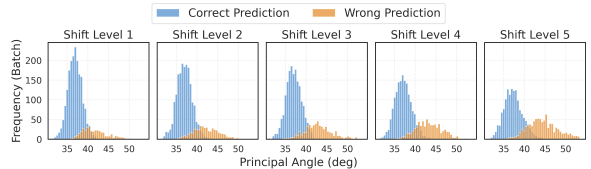


Figure 2: Principal angles (↓). **Correct predictions** exhibit consistently smaller principal angles than **mispredictions**. Increased shift level results in larger angles and more mispredictions.

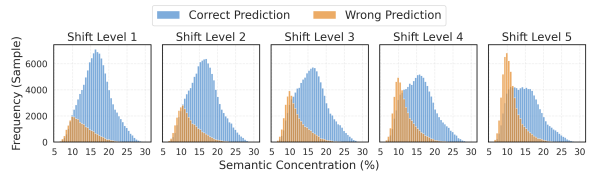


Figure 3: Semantic concentration (↑). **Correct predictions** exhibit markedly higher semantic concentration than **mispredictions**. Increased shift level results in lower concentration and more mispredictions.

trained vision-language geometry. Second (*Semantic Projection*), to eliminate visual nuisance, we project the aligned visual embeddings onto the task-specific textual subspace. The projection acts as a semantic filter which constrains visual features to lie within the semantic span defined by the textual basis, effectively discarding irrelevant noise and recovering the submerged semantic signal. Finally, standard self-training objectives are applied within this purified space to sharpen decision boundaries.

Our contributions are summarized as follows:

- **Analysis.** We provide a novel perspective on VLM TTA failure, identifying two barriers, namely modality gap and visual nuisance.
- **Method.** We propose SubTTA, a subspace-centric TTA framework to align visual-textual subspaces and filter visual nuisance via semantic projection, ensuring pseudo label quality.
- **Evaluation.** Extensive experiments on diverse benchmarks and VLM architectures demonstrate that SubTTA significantly outperforms state-of-the-art TTA methods.

## 2 Related Works

**Vision-Language Model Test-time Adaptation.** Existing VLM TTA methods broadly fall into two categories: *training-based* and *training-free* methods. *Training-based* approaches focus on updating model parameters or prompts during inference using self-supervised objectives. Early works such as TENT (Wang et al., 2020) and MEMO (Zhang et al., 2022) minimize the entropy of model predictions to reduce uncertainty. To improve sta-

bility against noisy pseudo-labels, RPL (Rusak et al., 2022) and RoTTA (Yuan et al., 2023) introduce robust loss function and batch normalization. Specific to VLMs, prompt-tuning approaches such as TPT (Shu et al., 2022) optimize learnable context prompts to adapt to downstream tasks. Recent studies have further diversified these optimization strategies. For instance, cluster-based methods like BATCLIP (Maharana et al., 2025) and MINT (Bao et al., 2025) leverage the cluster structure of test data to refine pseudo-labels. WATT (Osowiechi et al., 2024) utilizes model merging to average weights across adaptation steps, and PANDA (Deng et al., 2025) employs negative augmentation to alleviate shifts.

*Training-free* methods refine predictions without gradient updates, hence achieving lighter computational overhead. DMN (Zhang et al., 2024) and ECALP (Li et al., 2025a) calibrate the output distribution by adjusting logits or prototypes. ZERO (Farrera et al., 2024) and VTE (Döbler et al., 2024) align visual and textual features using closed-form solutions or heuristic statistics. TDA (Karmanov et al., 2024) further pushes the efficiency boundary by adjusting the feature distribution on-the-fly.

Despite their effectiveness, existing methods heavily rely on raw zero-shot predictions to guide adaptation, which can be noisy and may trigger catastrophic failures. To address this, our proposed SubTTA aims to refine zero-shot predictions to enable more robust and reliable TTA.

**Geometric Adaptation.** A growing area of interest exploits the geometric properties of the feature space to bridge the modality gap. SSP (Zhu et al., 2024) constructs vision and language subspaces through a selection projection mechanism, tailored specifically for the few-shot setting where labeled support sets are available. SSA (Adachi et al., 2025) proposes significant-subspace alignment designed for regression tasks, primarily focusing on uni-modal feature distributions. STS (Dafnis and Metaxas, 2025) employs a lightweight steering vector to adapt textual embeddings; while efficient, such unidirectional text-to-image alignment may inadvertently accommodate task-irrelevant visual nuisances present in the image embeddings.

### 3 Methodology

In this section, we introduce our proposed SubTTA to improve TTA performance via subspace alignment. We first introduce preliminaries in Sec-

tion 3.1. Afterwards, we introduce two key components, namely geometric alignment and semantic projection, in Sections 3.2 and 3.3, respectively.

#### 3.1 Preliminaries

We denote text space by  $\mathcal{T}$  and image space by  $\mathcal{V}$ . A VLM consisting of an image encoder  $f_v : \mathcal{V} \rightarrow \mathbb{R}^d$  and a text encoder  $f_t : \mathcal{T} \rightarrow \mathbb{R}^d$ , which aligns image and text embeddings in a shared space. For an image classification task with  $C$  classes, the text encoder  $f_t$  embeds the textual descriptions, e.g., "A photo of a <class>", into text embeddings  $\mathbf{t}_1, \dots, \mathbf{t}_C \in \mathbb{R}^d$ . Given a test image, the image encoder  $f_v$  embeds it into an image embedding  $\mathbf{v} \in \mathbb{R}^d$ , and the prediction corresponds to the class with the highest similarity score, i.e.,  $\arg \max_c \mathbf{v}^\top \mathbf{t}_c$ .

#### 3.2 Geometric Alignment

High-dimensional VLM embeddings are susceptible to the modality gap under distribution shifts, where structural misalignment leads to unreliable zero-shot predictions. To mitigate this, we propose to align the visual and textual representations within a refined low-dimensional subspace.

We begin by identifying the principal directions that capture textual and visual semantics via eigendecomposition on feature covariance matrices. For the textual modality, textual prompts encapsulate rich task-specific semantic information (e.g., class categories), hence their covariance matrix  $\Sigma_{\mathcal{T}}$  effectively defines the target semantic space. Formally, given the normalized text embeddings  $\mathbf{T} = [\mathbf{t}_1, \dots, \mathbf{t}_C]^\top \in \mathbb{R}^{C \times d}$ , the text covariance matrix is computed as  $\Sigma_{\mathcal{T}} = \mathbf{T}^\top \mathbf{T} \in \mathbb{R}^{d \times d}$ . For the visual modality, test images typically arrive in small batches, which provide insufficient statistics to accurately estimate the global visual distribution, leading to high estimation variance and noise (Bao et al., 2025). To mitigate such instability, we employ an Exponential Moving Average (EMA) to maintain a robust estimate of the visual covariance. Specifically, we initialize the visual covariance using the textual covariance as a semantic prior, i.e.,  $\Sigma_{\mathcal{V}} \leftarrow \Sigma_{\mathcal{T}}$ . For each step  $k$ , with the normalized image batch  $\mathbf{V}^{(k)} = [\mathbf{v}_1, \dots, \mathbf{v}_B]^\top \in \mathbb{R}^{B \times d}$ , the visual covariance matrix is gradually updated by

$$\Sigma_{\mathcal{V}} \leftarrow (1 - \alpha) \Sigma_{\mathcal{V}} + \alpha (\mathbf{V}^{(k)^\top} \mathbf{V}^{(k)}), \quad (1)$$

where  $\alpha$  is the momentum coefficient.

To extract the dominant components from the noisy covariance matrices, we perform eigende-

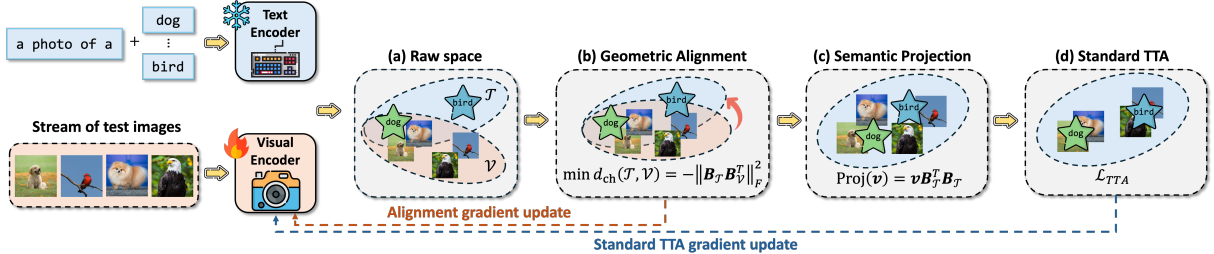


Figure 4: Overview of SubTTA. (a) VLM encodes images and textual prompts into a shared raw space. (b) Geometric alignment alleviates modality gap by minimizing the chordal distance. (c) Semantic projection retains task-relevant information, e.g., category, while filtering out irrelevant ones, e.g., background color. (d) Standard TTA is further performed on the aligned subspace.

composition to obtain the rank- $r$  approximations

$$\Sigma_T \approx \mathbf{B}_T^\top \Lambda_T \mathbf{B}_T, \Sigma_V \approx \mathbf{B}_V^\top \Lambda_V \mathbf{B}_V, \quad (2)$$

where  $\mathbf{B}_T, \mathbf{B}_V \in \mathbb{R}^{r \times d}$  are the top- $r$  orthonormal eigenvectors corresponding to the principal basis, and  $\Lambda_T, \Lambda_V$  are diagonal matrices containing the corresponding top- $r$  eigenvalues.

After obtaining the principal bases, we follow prior works (Osowiechi et al., 2024; Hakim et al., 2025; Bao et al., 2025) and adapt the normalization layers of the image encoder to align the visual span  $\mathbf{B}_V$  to the textual anchor  $\mathbf{B}_T$ . Conventional metrics, such as Frobenius norm  $\|\mathbf{B}_T - \mathbf{B}_V\|_F$  and cosine similarity  $\sum_{i=1}^r \mathbf{B}_T(i)^\top \mathbf{B}_V(i)$ , enforce a *rigid rank-to-rank alignment*, i.e., forcing  $\mathbf{B}_T(i)$  to align with  $\mathbf{B}_V(i)$ . However, this can be problematic because the bases in  $\mathbf{B}_T$  and  $\mathbf{B}_V$  are sorted by statistical variance rather than semantic relevance. For instance, the top-ranked visual basis may capture dominant but task-irrelevant signals (e.g., background intensity or style) rather than target objects. Consequently, enforcing a rigid rank-to-rank correspondence may erroneously align these nuisances with the primary textual anchors. Therefore, the distance metric is expected to be solely defined by the subspace geometry while remaining invariant to the specific choice of basis vectors.

To satisfy this property, we employ the chordal distance on the Grassmannian manifold as follows

$$d_{\text{ch}}(\mathbf{B}_T, \mathbf{B}_V) = \sqrt{\sum_{i=1}^r \sin^2 \theta_i}, \quad (3)$$

where  $\theta_i$  represents the  $i$ -th principal angle between subspaces  $\text{span}(\mathbf{B}_T)$  and  $\text{span}(\mathbf{B}_V)$ . Geometrically, minimizing the chordal distance forces the principal angles toward zero, thereby maximizing the overlap between the visual and textual subspaces. Based on this, we formulate our alignment

objective as the squared chordal distance, which can be efficiently computed via the Frobenius norm as follows (Conway et al., 1996)

$$\mathcal{L}_{\text{align}} = d_{\text{ch}}^2(\mathbf{B}_T, \mathbf{B}_V) = r - \|\mathbf{B}_T \mathbf{B}_V^\top\|_F^2. \quad (4)$$

Note that the chordal distance is defined solely by the principal angles  $\{\theta_i\}_{i=1}^r$  between the two subspaces, remaining invariant to the basis choices. Formally, consider an orthogonal rotation matrix  $\mathbf{Q} \in \mathbb{R}^{r \times r}$  with  $\mathbf{Q}^\top \mathbf{Q} = \mathbf{I}$  that rotates the visual bases by  $\mathbf{Q} \mathbf{B}_V$ , we have

$$\begin{aligned} \|\mathbf{B}_T(\mathbf{Q} \mathbf{B}_V)^\top\|_F^2 &= \text{Tr} \left( \mathbf{B}_T \mathbf{B}_V^\top \mathbf{Q}^\top \mathbf{Q} \mathbf{B}_V \mathbf{B}_T^\top \right) \\ &= \text{Tr} \left( \mathbf{B}_T \mathbf{B}_V^\top \mathbf{B}_V \mathbf{B}_T^\top \right) \\ &= \|\mathbf{B}_T \mathbf{B}_V^\top\|_F^2. \end{aligned}$$

This geometric flexibility avoids rigid rank-to-rank alignment, and enables a global matching that allows relevant visual signals to align with the correct textual anchors regardless of their rank order.

### 3.3 Semantic Projection

While geometric alignment effectively rectifies the global distribution drift, it preserves the intrinsic structure of the visual features that include the task-irrelevant nuisance. To eliminate such nuisance, we leverage the textual subspace, which is compact and rich in task-specific semantics, as a hard semantic filter. Specifically, for image embedding  $\mathbf{v}$ , the semantic projection is defined as follows

$$\text{Proj}(\mathbf{v}) = \mathbf{v} \mathbf{B}_T^\top \mathbf{B}_T. \quad (5)$$

This operation effectively discards noises orthogonal to the semantic span, yielding a purified embedding space that facilitates high-quality zero-shot predictions. Equipped with the purified embeddings, SubTTA can be seamlessly integrated with various TTA objectives (e.g., entropy-based or cluster-based) to refine decision boundaries.

Table 1: Benchmark results with ViT-B-16. We denote Top-1/2/3 by Blue/Yellow/red, respectively.

Method	Noise			Blur				Weather				Digital				Mean	
	Gauss.	Shot	Impul.	Defoc.	Glass	Motion	Zoom	Snow	Frost	Fog	Brit.	Contr.	Elast.	Pixel.	JPEG		
ImageNet-C	Source	11.14	12.54	12.06	23.34	15.26	24.44	22.72	32.36	29.86	35.94	54.08	17.26	12.70	31.00	33.34	24.54
	TDA	12.42	14.80	14.80	23.70	16.70	26.06	23.98	33.54	32.10	38.00	55.28	19.32	14.18	33.46	34.98	26.22
	DMN	11.50	14.14	14.00	22.32	15.78	24.56	22.54	31.52	30.36	35.34	54.24	16.30	12.48	32.52	24.79	24.16
	VTE	9.18	10.80	10.80	24.70	14.36	24.28	25.20	35.40	32.44	38.20	55.52	16.20	14.34	38.68	34.04	25.61
	ZERO	10.50	11.50	11.12	24.78	14.88	24.36	23.28	33.04	30.40	37.06	54.52	16.90	13.40	34.90	32.90	24.90
	ECALP	13.34	15.58	14.10	22.56	15.56	25.52	23.64	30.96	30.02	35.78	52.08	18.34	13.52	33.14	33.30	25.16
	TENT	5.20	5.68	7.42	25.30	19.34	26.86	24.16	33.52	30.54	37.80	54.32	22.52	13.90	35.08	36.02	25.18
	RoTTA	11.44	13.08	12.36	23.46	15.48	24.66	22.78	32.60	29.92	35.86	54.18	17.34	12.92	31.02	33.52	24.71
	TPT	8.54	9.44	10.16	24.06	15.06	25.00	24.04	33.96	32.18	37.08	55.52	16.52	13.68	33.90	33.56	24.85
	MEMO	11.08	12.38	12.02	23.54	15.44	24.60	22.90	32.54	30.06	35.94	54.02	17.46	12.80	31.24	33.40	24.63
CIFAR10-C	WATT	11.18	12.78	13.02	25.12	18.08	26.90	25.22	33.42	30.22	37.40	53.96	21.84	15.16	33.46	34.94	26.18
	MINT	19.68	20.36	19.44	26.88	21.52	29.88	25.96	32.68	29.38	38.84	55.10	24.30	19.06	36.38	38.24	29.18
	BATCLIP	19.48	21.02	19.30	25.92	21.26	29.96	28.52	35.22	31.38	40.24	55.20	25.68	23.72	36.82	37.22	30.06
	SubTTA	21.16	22.88	21.44	25.34	24.82	30.70	29.64	37.24	35.90	41.26	56.96	29.74	29.40	37.58	38.18	32.15
	Source	37.94	41.68	54.44	71.73	40.87	67.90	73.67	73.88	77.34	70.25	84.41	62.41	53.81	47.66	59.45	61.16
CIFAR100-C	TDA	40.91	44.31	50.45	72.80	44.38	71.60	75.97	75.29	77.84	71.75	86.07	62.34	56.34	47.77	57.68	62.37
	DMN	43.34	47.52	54.11	73.43	39.99	72.25	75.97	74.31	76.46	71.24	84.54	60.56	54.15	47.20	57.14	62.15
	VTE	42.34	46.22	64.25	71.14	45.63	68.51	73.66	76.74	78.27	71.06	85.27	57.24	59.62	60.59	61.89	64.16
	ZERO	39.22	43.77	57.19	71.91	40.71	69.22	74.11	74.36	77.24	72.44	83.85	60.74	55.64	48.97	62.29	62.11
	ECALP	46.52	50.81	61.04	71.83	41.52	70.48	75.38	75.82	78.99	71.24	86.03	60.70	58.06	49.78	61.17	63.96
	TENT	15.42	18.30	38.18	81.43	21.54	76.33	82.24	83.59	82.24	80.56	89.76	80.65	63.50	58.83	56.27	61.92
	RoTTA	39.20	42.64	55.33	72.10	41.20	68.11	74.02	74.39	78.02	70.78	84.77	63.09	54.61	49.44	60.12	61.85
	TPT	37.76	42.19	60.66	72.84	44.82	69.72	75.37	75.95	78.90	72.15	85.67	62.04	58.86	55.18	62.58	63.65
	MEMO	37.61	41.26	55.64	72.08	41.58	68.60	73.97	74.96	77.34	71.50	84.79	62.07	55.50	49.23	61.02	61.81
	WATT	45.98	53.25	60.31	74.99	38.58	71.49	75.92	77.69	80.23	76.33	87.56	75.59	55.42	62.04	63.21	66.57
CIFAR100-C	MINT	54.40	58.73	64.53	76.54	48.90	77.89	79.27	81.58	81.51	77.20	89.94	74.54	62.11	61.42	64.45	70.20
	BATCLIP	61.89	65.44	67.07	80.06	55.47	80.02	81.60	82.47	83.69	80.43	88.47	81.19	69.12	62.67	67.29	73.79
	SubTTA	60.18	66.62	69.73	81.47	59.94	81.24	82.39	83.72	83.75	83.48	91.42	86.26	70.94	74.42	69.41	76.33

## 4 Experiments

We carry out extensive experiments to answer the following research questions, including

- RQ1:** How effective is SubTTA against distribution shifts? (Sections 4.2 & 4.3)
- RQ2:** How does SubTTA improve zero-shot predictions? (Section 4.4)
- RQ3:** How robust is SubTTA to hyperparameter choices and shift levels? (Section 4.5)

### 4.1 Experiment Setup

**Datasets and Metric.** We evaluate SubTTA on three corrupted image classification benchmarks: CIFAR-10-C (Krizhevsky et al., 2009), CIFAR-100-C (Hendrycks and Dietterich, 2019), and ImageNet-C (Deng et al., 2009), which include 15 distinct types of corruptions. We adopt the classification accuracy as the evaluation metric.

**CLIP Models.** We consider the following widely used CLIP (Radford et al., 2021) models, including ViT-B-16, ViT-B-32, and ViT-L-14.

**Baseline TTA Methods.** We benchmark SubTTA against state-of-the-art TTA approaches. *Training-*

*free methods* include memory-based methods (TDA (Karmanov et al., 2024), DMN (Zhang et al., 2024), ECALP (Li et al., 2025a)) that leverage sample similarity to adjust predictions, and augmentation-based methods (VTE (Döbler et al., 2024), ZERO (Farina et al., 2024)) that aggregate image embeddings from multiple augmentations. *Training-based methods* include entropy-based methods (MEMO (Zhang et al., 2022), WATT (Osowiechi et al., 2024), RoTTA (Yuan et al., 2023), TPT (Shu et al., 2022)), and cluster-based methods (MINT (Bao et al., 2025), BATCLIP (Maharana et al., 2025)).

**SubTTA Variants.** In the benchmark experiments, we primarily employ the inter-class variance loss from MINT (Bao et al., 2025) as the TTA objective on the purified embeddings. In the following study, we also experiment with other TTA objectives to evaluate the versatility of SubTTA in Section 4.3.

**Experiment Pipeline.** Following the established TTA protocol (Wang et al., 2020), we conduct experiments under the highest severity level (Level 5)

to simulate severe distribution shifts. We adopt an online adaptation setting where the model adapts to a continuous stream of unlabeled test data for each corruption type independently, resetting the model state between corruptions. All experiments are executed on NVIDIA A100 80GB GPUs.

## 4.2 Benchmark Results

We conduct experiments on three corruption benchmarks, and report the results with ViT-B-16 in Table 1. Additional results with ViT-B-32 and ViT-L-14 models are reported in Tables 2 and 3 in Appendix A, respectively.

### (1) SubTTA establishes a new state-of-the-art with consistent robustness.

SubTTA consistently delivers the strongest overall performance across diverse benchmarks. In fine-grained settings, SubTTA consistently ranks within the Top-3 and achieves the best performance in the majority of scenarios. On the large-scale ImageNet-C dataset, SubTTA achieves a mean accuracy of 32.15%, surpassing the previous best method BATCLIP (30.06%) by a significant margin of 2.09%. Such superiority is equally pronounced on smaller-resolution benchmarks: SubTTA outperforms the best competitor by 2.54% on CIFAR-10-C, and 2.08% on CIFAR-100-C. This validates that SubTTA constructs a geometrically rectified feature space that is inherently more robust to varying forms of distribution shifts.

### (2) SubTTA eliminates negative adaptation and ensures stability.

Existing baseline methods often suffer from catastrophic failure under large shifts, leading to negative adaptation where performance drops below the source CLIP baseline. For instance, we observe that TENT fails to adapt to noise corruptions due to unstable entropy minimization, while DMN often struggles with digital corruptions. SubTTA exhibits remarkable resilience, consistently outperforming the source CLIP model across every corruption category. This stability confirms that our subspace alignment effectively filters out the nuisance factors that typically destabilize other adaptation algorithms.

## 4.3 Performance with Various TTA Objectives

Our proposed SubTTA is compatible with various TTA objectives. To validate this, we integrate SubTTA with three categories of baseline methods, including Source CLIP model, entropy minimization (TENT), cluster-based methods (MINT, BATCLIP), and the results are shown in Figure 5.

First, SubTTA acts as a universal performance,

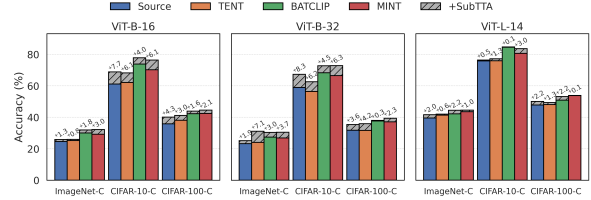


Figure 5: TTA performance w/ and w/o SubTTA.

irrespective of the adaptation objective. When integrated with diverse TTA strategies, SubTTA consistently yields performance improvements. This indicates that SubTTA effectively rectifies the underlying structure before standard TTA is applied.

Second, we observe more pronounced performance gains on lower-capacity models (e.g., ViT-B-16 and ViT-B-32) compared to stronger ones (e.g., ViT-L-14). We attribute this to the fact that weaker models are inherently more susceptible to modality gap and distribution shifts. SubTTA effectively compensates for these intrinsic representational deficits, providing critical robustness where the pre-trained alignment is most fragile.

## 4.4 On Improving Zero-shot Prediction

In this section, we empirically validate the mechanisms through which SubTTA enhances the zero-shot prediction capability of CLIP. Figure 6 visualizes the distributions of three key metrics, including principal angle, semantic concentration, and visual-textual similarity. Comparing the baseline CLIP model with our SubTTA-augmented version, we draw the following observations.

**(1) SubTTA rectifies modality gap.** We first examine the modality gap by analyzing the principal angles between the visual and textual subspaces. As shown in Figure 6a, CLIP without SubTTA exhibits relatively large principal angles, indicating that distribution shifts induce a significant misalignment between the visual features and their corresponding textual anchors. In contrast, applying SubTTA leads to a marked reduction in principal angles across all datasets. Such reduction demonstrates that SubTTA effectively rectifies the modality gap, pulling the drifted visual manifold back into geometric alignment with the invariant textual semantic space, thereby ensuring more reliable cross-modal matching.

**(2) SubTTA alleviates visual nuisance.** We then investigate visual nuisance by measuring semantic concentration, the ratio of visual energy preserved within the task-specific textual subspace. As shown in Figure 6b, CLIP without SubTTA exhibits a distri-

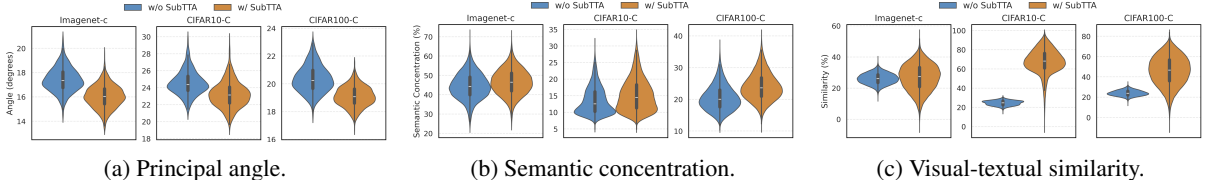


Figure 6: Study on improving zero-shot predictions. Blue denote source **CLIP w/o SubTTA** and Orange denote **CLIP w/ SubTTA**. (a) Principal angles ( $\downarrow$ ): SubTTA mitigates modality gap; (b) Semantic concentration ( $\uparrow$ ): SubTTA alleviates visual nuisance; (c) Visual-textual similarity ( $\uparrow$ ): SubTTA improves pseudo-label quality.

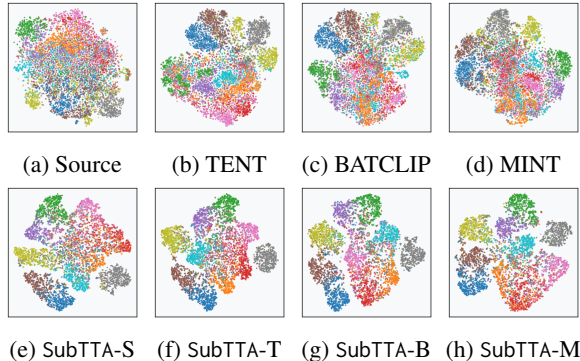


Figure 7: CIFAR-10-C embedding visualization of different TTA methods w/o (a-d) and w/ (e-h) SubTTA.

bution skewed toward the lower end of the semantic concentration spectrum. This indicates that in the raw feature space, the task-relevant semantic signal is largely overwhelmed by orthogonal components, which correspond to task-irrelevant nuisances such as background clutter or domain-specific styles. Conversely, SubTTA propels the entire distribution toward the high-concentration regime, demonstrating that the adapted features are better aligned with the textual semantic span.

**(3) SubTTA improves pseudo-label quality.** We also assess pseudo-label quality by analyzing the cosine similarity between visual embeddings and their corresponding ground-truth textual prompts. As shown in Figure 6c, CLIP without SubTTA suffers from low visual-textual similarity scores, reflecting weak confidence in the correct semantic alignment. However, SubTTA significantly shifts the similarities toward higher values. This increase indicates that the rectified visual features possess much higher semantic fidelity to their true labels. Consequently, the zero-shot predictions derived from these enhanced similarities are not only more accurate but also more confident, providing high-quality pseudo-labels that are critical for preventing error accumulation during test-time adaptation.

**(4) SubTTA enhances embedding quality.** In addition, we visualize the learned representations of CIFAR-10-C with and without SubTTA using t-

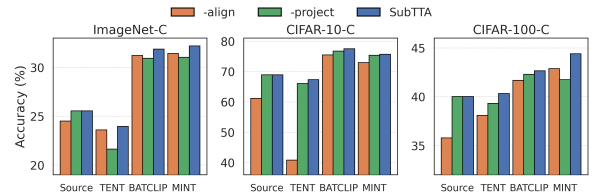


Figure 8: Ablation study on alignment and projection.

SNE, and the results are shown in Figure 7. As shown in the top row of Figure 7, the embeddings extracted by baselines are severely entangled, exhibiting blurred decision boundaries and cluster overlap. This indicates a failure to disentangle task-relevant semantics from shift-induced noise, resulting in compromised discriminative power. In contrast, integrating SubTTA (bottom row) induces a profound geometric rectification. First, SubTTA significantly improves *intra-class compactness*, where dispersed features are pulled tighter together. Second, SubTTA enhances *inter-class separability*, effectively pushing apart overlapping manifolds to form clear margins between categories. This visualization validates our motivation: by projecting features onto the aligned subspace, SubTTA effectively filters out task-irrelevant nuisances and restores a discriminative semantic structure.

## 4.5 Studies

We carry out ablation study and hyperparameter study on ImageNet-C dataset with ViT-B-16 model.

### 4.5.1 Ablation Study

We investigate the contributions of geometric alignment and semantic projection in Figure 8, denoting their ablated versions as *-align* and *-project*, respectively. We draw the following observations.

**(1) Alignment is a prerequisite for projection.** The significant drop in *-align* indicates that projection is only valid when subspaces are aligned; otherwise, features may be mapped to incorrect semantic bases. Notably, TENT suffers from negative transfer w/o alignment, as naive projection creates confidently-wrong predictions that mislead entropy minimization.

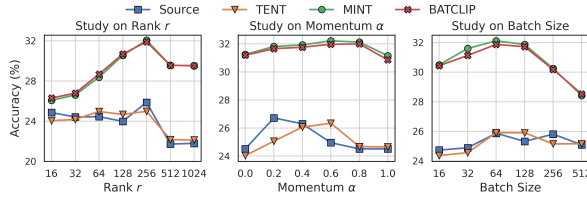


Figure 9: Hyper-parameter study. Different curves represent SubTTA with different TTA objectives.

**(2) Projection is a semantic denoiser.** The performance gap between -project and SubTTA confirms that raw embeddings contain task-irrelevant nuisances. Semantic projection effectively filters these dimensions, constructing a purified space that prevents optimization on spurious correlations.

**(3) Synergy of components.** SubTTA consistently outperforms both variants, confirming neither is redundant. Alignment corrects global modality drift while projection filters local visual nuisances; both are indispensable for optimal adaptation.

#### 4.5.2 Hyperparameter Study

We investigate the sensitivity of SubTTA to three key hyperparameters: the subspace rank  $r$ , the momentum coefficient  $\alpha$  and batch size. The results are shown in Figure 9.

**Impact of subspace rank  $r$ .** When subspace rank  $r$  increases, the accuracy first increases then decreases. With small rank (e.g.,  $r < 64$ ), the performance is suboptimal because the subspace is overly compressed, causing the loss of critical semantic information. Conversely, performance degradation is observed when  $r$  approaches the full feature dimension (i.e.,  $d = 512$  for ViT-B-16). We attribute this to the fact that a full-rank subspace preserves all trailing principal components, hence task-irrelevant nuisances are not filtered out, which negates the denoising benefits of our subspace approach.

**Impact of momentum coefficient  $\alpha$ .** Results show that SubTTA is generally robust for  $\alpha \in (0.2, 0.8)$ . However, performance drops significantly at the extremes. When  $\alpha = 0$ , the covariance estimation relies entirely on the current mini-batch. This introduces instability due to the high variance of statistics estimated from small batches, failing to capture the global visual distribution. When  $\alpha = 1$ , the visual covariance is fixed to the initial textual prior  $\Sigma_T$  and never updates with visual features. In this scenario, the subspace alignment mechanism is effectively disabled, leading to a marked performance drop. This confirms the necessity of our momentum-based update strategy.

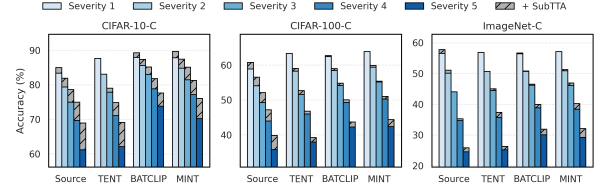


Figure 10: TTA performance under different shift levels.

**Impact of batch size.** As batch size increases, the accuracy first increases then saturates or decreases. With small batch sizes (e.g.,  $B = 16$ ), the estimated visual covariance matrix becomes statistically unreliable and prone to high variance, causing the subspace alignment to fluctuate erratically based on local sample noise rather than the true manifold geometry. Conversely, larger batch sizes provide better covariance estimation for accurate manifold matching, though the marginal gains diminish once statistical stability is reached. This validates that sufficient sampling is critical for robust geometric rectification.

#### 4.5.3 Robustness against Shift Levels

We evaluate how model performs under different shift levels, and the results are shown in Figure 10. First, we observe a consistent performance degradation in all baseline methods (colored bars) as severity increases, confirming the vulnerability of pre-trained CLIP models to severe distribution shifts. Second, the efficacy of SubTTA correlates positively with shift severity. While the improvements are consistent at lower levels, the performance boost (hatched bars) becomes more significant at higher levels. This indicates that SubTTA is particularly critical in extreme scenarios, effectively acting as a safeguard where standard baselines struggle most.

## 5 Conclusion

In this work, we address the vulnerability of VLMs to distribution shifts by investigating the prevalent yet precarious reliance on raw zero-shot predictions. We identify that adaptation failures stem from modality gap and visual nuisance within the shifted embedding space. To overcome these barriers, we propose SubTTA, a novel framework that shifts the TTA from noisy self-training to robust subspace geometry. By explicitly aligning the visual subspace to the textual semantic anchor via chordal distance and projecting features onto a purified task-specific subspace, SubTTA effectively rectifies modality gap and alleviates visual nuisance. Extensive experiments validate the effectiveness of SubTTA in enhancing various TTA methods.

## Limitations

While SubTTA demonstrates robust performance, we acknowledge a few limitations. First, our method relies on batch-level statistics to estimate reliable subspaces. Consequently, it is not immediately applicable to the strictly episodic setting, where model is adapted to a single test sample, without a mechanism to accumulate historical samples (e.g., a memory bank). Second, as an optimization-based approach, SubTTA requires open-source model with access to model gradients, restricting its usage with closed-source proprietary APIs. Lastly, the SVD operation introduces a slight computational overhead compared to training-free baselines. Future work could explore efficient approximations for eigendecomposition to further reduce latency, or extend the subspace alignment principle to black-box adaptation scenarios.

## References

Josh Achiam, Steven Adler, Sandhini Agarwal, Lama Ahmad, Ilge Akkaya, Florencia Leoni Aleman, Diogo Almeida, Janko Altenschmidt, Sam Altman, Shyamal Anadkat, and 1 others. 2023. Gpt-4 technical report. *arXiv preprint arXiv:2303.08774*.

Kazuki Adachi, Shin’ya Yamaguchi, Atsutoshi Kumagai, and Tomoki Hamagami. 2025. Test-time adaptation for regression by subspace alignment. In *The Thirteenth International Conference on Learning Representations*.

Sravanti Addepalli, Ashish Ramayee Asokan, Lakshay Sharma, and R Venkatesh Babu. 2024. Leveraging vision-language models for improving domain generalization in image classification. In *Proceedings of the IEEE/CVF Conference on Computer Vision and Pattern Recognition*, pages 23922–23932.

Mengting Ai, Tianxin Wei, Yifan Chen, Zhichen Zeng, Ritchie Zhao, Girish Varatkar, Bita Darvish Rouhani, Xianfeng Tang, Hanghang Tong, and Jingrui He. 2025. Resmoe: Space-efficient compression of mixture of experts llms via residual restoration. *arXiv preprint arXiv:2503.06881*.

Jean-Baptiste Alayrac, Jeff Donahue, Pauline Luc, Antoine Miech, Iain Barr, Yana Hasson, Karel Lenc, Arthur Mensch, Katherine Millican, Malcolm Reynolds, and 1 others. 2022. Flamingo: a visual language model for few-shot learning. *Advances in neural information processing systems*, 35:23716–23736.

Wenxuan Bao, Ruxi Deng, and Jingrui He. 2025. Mint: A simple test-time adaptation of vision-language models against common corruptions. *arXiv preprint arXiv:2510.22127*.

Wenxuan Bao, Zhichen Zeng, Zhining Liu, Hanghang Tong, and Jingrui He. 2024. Matcha: Mitigating graph structure shifts with test-time adaptation. *arXiv preprint arXiv:2410.06976*.

Liqun Chen, Zhe Gan, Yu Cheng, Linjie Li, Lawrence Carin, and Jingjing Liu. 2020. Graph optimal transport for cross-domain alignment. In *International Conference on Machine Learning*, pages 1542–1553. PMLR.

Xi Chen, Xiao Wang, Soravit Changpinyo, Anthony J Piergiovanni, Piotr Padlewski, Daniel Salz, Sebastian Goodman, Adam Grycner, Basil Mustafa, Lucas Beyer, and 1 others. 2022. Pali: A jointly-scaled multilingual language-image model. *arXiv preprint arXiv:2209.06794*.

John H Conway, Ronald H Hardin, and Neil JA Sloane. 1996. Packing lines, planes, etc.: Packings in grassmannian spaces. *Experimental mathematics*, 5(2):139–159.

Chengming Cui, Tianxin Wei, Ziyi Chen, Ruizhong Qiu, Zhichen Zeng, Zhining Liu, Xuying Ning, Duo Zhou, and Jingrui He. 2026. Adafuse: Adaptive ensemble decoding with test-time scaling for llms. *Preprint*, arXiv:2601.06022.

Konstantinos M Dafnis and Dimitris N Metaxas. 2025. Test-time spectrum-aware latent steering for zero-shot generalization in vision-language models. In *The Thirty-ninth Annual Conference on Neural Information Processing Systems*.

Jia Deng, Wei Dong, Richard Socher, Li-Jia Li, Kai Li, and Li Fei-Fei. 2009. Imagenet: A large-scale hierarchical image database. In *2009 IEEE conference on computer vision and pattern recognition*, pages 248–255. Ieee.

Ruxi Deng, Wenxuan Bao, Tianxin Wei, and Jingrui He. 2025. Panda: Test-time adaptation with negative data augmentation. *arXiv preprint arXiv:2511.10481*.

Mario Döbler, Robert A Marsden, Tobias Raichle, and Bin Yang. 2024. A lost opportunity for vision-language models: a comparative study of online test-time adaptation for vision-language models. In *European Conference on Computer Vision*, pages 117–133. Springer.

Boxin Du, Si Zhang, Yuchen Yan, and Hanghang Tong. 2021. New frontiers of multi-network mining: Recent developments and future trend. In *Proceedings of the 27th ACM SIGKDD Conference on Knowledge Discovery & Data Mining*, pages 4038–4039.

Matteo Farina, Gianni Franchi, Giovanni Iacca, Massimiliano Mancini, and Elisa Ricci. 2024. Frustratingly easy test-time adaptation of vision-language models. *Advances in Neural Information Processing Systems*, 37:129062–129093.

Basura Fernando, Amaury Habrard, Marc Sebban, and Tinne Tuytelaars. 2013. Unsupervised visual domain adaptation using subspace alignment. In *Proceedings of the IEEE international conference on computer vision*, pages 2960–2967.

Yaroslav Ganin and Victor Lempitsky. 2015. Unsupervised domain adaptation by backpropagation. In *International conference on machine learning*, pages 1180–1189. PMLR.

Boqing Gong, Yuan Shi, Fei Sha, and Kristen Grauman. 2012. Geodesic flow kernel for unsupervised domain adaptation. In *2012 IEEE conference on computer vision and pattern recognition*, pages 2066–2073. IEEE.

Gustavo A Vargas Hakim, David Osowiecki, Mehrdad Noori, Milad Cheraghalkhani, Ali Bahri, Moslem Yazdanpanah, Ismail Ben Ayed, and Christian Desrosiers. 2025. Clipartt: Adaptation of clip to new domains at test time. In *2025 IEEE/CVF Winter Conference on Applications of Computer Vision (WACV)*, pages 7092–7101. IEEE.

Dan Hendrycks and Thomas Dietterich. 2019. Benchmarking neural network robustness to common corruptions and perturbations. *arXiv preprint arXiv:1903.12261*.

Ngoc Dung Huynh, Mohamed Reda Bouadjenek, Sunil Aryal, Imran Razzak, and Hakim Hacid. 2025. Visual question answering: from early developments to recent advances—a survey. *arXiv preprint arXiv:2501.03939*.

Chao Jia, Yafei Yang, Ye Xia, Yi-Ting Chen, Zarana Parekh, Hieu Pham, Quoc Le, Yun-Hsuan Sung, Zhen Li, and Tom Duerig. 2021. Scaling up visual and vision-language representation learning with noisy text supervision. In *International conference on machine learning*, pages 4904–4916. PMLR.

Baoyu Jing, Sanhorn Chen, Lecheng Zheng, Boyu Liu, Zihao Li, Jiaru Zou, Tianxin Wei, Zhining Liu, Zhichen Zeng, Ruizhong Qiu, and 1 others. Trqa: Time series reasoning question and answering benchmark.

Guoliang Kang, Lu Jiang, Yi Yang, and Alexander G Hauptmann. 2019. Contrastive adaptation network for unsupervised domain adaptation. In *Proceedings of the IEEE/CVF conference on computer vision and pattern recognition*, pages 4893–4902.

Adilbek Karmanov, Dayan Guan, Shijian Lu, Abdulmotaleb El Saddik, and Eric Xing. 2024. Efficient test-time adaptation of vision-language models. In *Proceedings of the IEEE/CVF Conference on Computer Vision and Pattern Recognition*, pages 14162–14171.

Alex Krizhevsky, Geoffrey Hinton, and 1 others. 2009. Learning multiple layers of features from tiny images.

Junnan Li, Dongxu Li, Silvio Savarese, and Steven Hoi. 2023. Blip-2: Bootstrapping language-image pre-training with frozen image encoders and large language models. In *International conference on machine learning*, pages 19730–19742. PMLR.

Yushu Li, Yongyi Su, Adam Goodge, Kui Jia, and Xun Xu. 2025a. Efficient and context-aware label propagation for zero-/few-shot training-free adaptation of vision-language model. In *The Thirteenth International Conference on Learning Representations*.

Zihao Li, Xiao Lin, Zhining Liu, Jiaru Zou, Ziwei Wu, Lecheng Zheng, Dongqi Fu, Yada Zhu, Hendrik Hamann, Hanghang Tong, and 1 others. 2025b. Language in the flow of time: Time-series-paired texts weaved into a unified temporal narrative. *arXiv preprint arXiv:2502.08942*.

Zihao Li, Xiao Lin, Zhining Liu, Jiaru Zou, Ziwei Wu, Lecheng Zheng, Dongqi Fu, Yada Zhu, Hendrik F. Hamann, Hanghang Tong, and Jingrui He. 2025c. Language in the flow of time: Time-series-paired texts weaved into a unified temporal narrative. *CoRR*, abs/2502.08942.

Zihao Li, Xiao Lin, Zhining Liu, Jiaru Zou, Ziwei Wu, Lecheng Zheng, Dongqi Fu, Yada Zhu, Hendrik F. Hamann, Hanghang Tong, and Jingrui He. 2025d. Language in the flow of time: Time-series-paired texts weaved into a unified temporal narrative. *CoRR*, abs/2502.08942.

Zihao Li, Lecheng Zheng, Bowen Jin, Dongqi Fu, Baoyu Jing, Yikun Ban, Jingrui He, and Jiawei Han. 2025e. Can graph neural networks learn language with extremely weak text supervision? In *Proceedings of the 63rd Annual Meeting of the Association for Computational Linguistics (Volume 1: Long Papers)*, ACL 2025, Vienna, Austria, July 27 - August 1, 2025, pages 11138–11165. Association for Computational Linguistics.

Mingfu Liang, Xi Liu, Rong Jin, Boyang Liu, Qiuling Suo, Qinghai Zhou, Song Zhou, Laming Chen, Hua Zheng, Zhiyuan Li, and 1 others. 2025. External large foundation model: How to efficiently serve trillions of parameters for online ads recommendation. In *Companion Proceedings of the ACM on Web Conference 2025*, pages 344–353.

Haokun Lin, Haobo Xu, Yichen Wu, Jingzhi Cui, Yingtao Zhang, Linzhan Mou, Linqi Song, Zhenan Sun, and Ying Wei. 2024a. Duquant: Distributing outliers via dual transformation makes stronger quantized llms. *Advances in Neural Information Processing Systems*, 37:87766–87800.

Haokun Lin, Haobo Xu, Yichen Wu, Ziyu Guo, Renrui Zhang, Zhichao Lu, Ying Wei, Qingfu Zhang, and Zhenan Sun. 2025a. Quantization meets dllms: A systematic study of post-training quantization for diffusion llms. *arXiv preprint arXiv:2508.14896*.

Xiao Lin, Jian Kang, Weilin Cong, and Hanghang Tong. 2024b. Bemap: Balanced message passing for fair graph neural network. In *Learning on Graphs Conference*, pages 37–1. PMLR.

Xiao Lin, Mingjie Li, and Yisen Wang. 2024c. Made: Graph backdoor defense with masked unlearning. *arXiv preprint arXiv:2411.18648*.

Xiao Lin, Philip Li, Zhichen Zeng, Tingwei Li, Tianxin Wei, Xuying Ning, Gaotang Li, Yuzhong Chen, and Hanghang Tong. 2026. Alert: Zero-shot llm jailbreak detection via internal discrepancy amplification. *arXiv preprint arXiv:2601.03600*.

Xiao Lin, Zhining Liu, Dongqi Fu, Ruizhong Qiu, and Hanghang Tong. 2024d. Backtime: Backdoor attacks on multivariate time series forecasting. *Advances in Neural Information Processing Systems*, 37:131344–131368.

Xiao Lin, Zhining Liu, Ze Yang, Gaotang Li, Ruizhong Qiu, Shuke Wang, Hui Liu, Haotian Li, Sumit Keswani, Vishwa Pardeshi, and 1 others. 2025b. Moralise: A structured benchmark for moral alignment in visual language models. *arXiv preprint arXiv:2505.14728*.

Xiao Lin, Zhichen Zeng, Tianxin Wei, Zhining Liu, Hanghang Tong, and 1 others. 2025c. Cats: Mitigating correlation shift for multivariate time series classification. *arXiv preprint arXiv:2504.04283*.

Haotian Liu, Chunyuan Li, Qingyang Wu, and Yong Jae Lee. 2023. Visual instruction tuning. *Advances in neural information processing systems*, 36:34892–34916.

Xiaolong Liu, Zhichen Zeng, Xiaoyi Liu, Siyang Yuan, Weinan Song, Mengyue Hang, Yiqun Liu, Chaofei Yang, Donghyun Kim, Wen-Yen Chen, and 1 others. 2024. A collaborative ensemble framework for ctr prediction. *arXiv preprint arXiv:2411.13700*.

Yahao Liu, Jinhong Deng, Xinchen Gao, Wen Li, and Lixin Duan. 2021. Bapa-net: Boundary adaptation and prototype alignment for cross-domain semantic segmentation. In *Proceedings of the IEEE/CVF international conference on computer vision*, pages 8801–8811.

Zhining Liu, Ze Yang, Xiao Lin, Ruizhong Qiu, Tianxin Wei, Yada Zhu, Hendrik Hamann, Jingrui He, and Hanghang Tong. 2025. Breaking silos: Adaptive model fusion unlocks better time series forecasting. *arXiv preprint arXiv:2505.18442*.

Mingsheng Long, Yue Cao, Jianmin Wang, and Michael Jordan. 2015. Learning transferable features with deep adaptation networks. In *International conference on machine learning*, pages 97–105. PMLR.

Sarthak Maharana, Baoming Zhang, Leonid Karlinsky, Rogerio Feris, and Yunhui Guo. 2025. Batclip: Bi-modal online test-time adaptation for clip. In *Proceedings of the IEEE/CVF International Conference on Computer Vision*, pages 1569–1579.

Saeid Motian, Marco Piccirilli, Donald A Adjeroh, and Gianfranco Doretto. 2017. Unified deep supervised domain adaptation and generalization. In *Proceedings of the IEEE international conference on computer vision*, pages 5715–5725.

David Osowiecki, Mehrdad Noori, Gustavo Vargas Hakim, Moslem Yazdanpanah, Ali Bahri, Mihad Cheraghali, Sahar Dastani, Farzad Beizaei, Ismail Ayed, and Christian Desrosiers. 2024. Watt: Weight average test time adaptation of clip. *Advances in neural information processing systems*, 37:48015–48044.

Or Patashnik, Zongze Wu, Eli Shechtman, Daniel Cohen-Or, and Dani Lischinski. 2021. Styleclip: Text-driven manipulation of stylegan imagery. In *Proceedings of the IEEE/CVF international conference on computer vision*, pages 2085–2094.

Xiangyu Qi, Kaixuan Huang, Ashwinee Panda, Peter Henderson, Mengdi Wang, and Prateek Mittal. 2024. Visual adversarial examples jailbreak aligned large language models. In *Proceedings of the AAAI conference on artificial intelligence*, volume 38, pages 21527–21536.

Ruizhong Qiu, Jun-Gi Jang, Xiao Lin, Lihui Liu, and Hanghang Tong. 2025. Tucket: A tensor time series data structure for efficient and accurate factor analysis over time ranges. *arXiv preprint arXiv:2501.06647*.

Alec Radford, Jong Wook Kim, Chris Hallacy, Aditya Ramesh, Gabriel Goh, Sandhini Agarwal, Girish Sastry, Amanda Askell, Pamela Mishkin, Jack Clark, and 1 others. 2021. Learning transferable visual models from natural language supervision. In *International conference on machine learning*, pages 8748–8763. PMLR.

Shane Roach, Connie Ni, Alexei Kopylov, Tsai-Ching Lu, Jiejun Xu, Si Zhang, Boxin Du, Dawei Zhou, Jun Wu, Lihui Liu, and 1 others. 2020. Canon: Complex analytics of network of networks for modeling adversarial activities. In *2020 IEEE International Conference on Big Data (Big Data)*, pages 1634–1643. IEEE.

Evgenia Rusak, Steffen Schneider, George Pachitariu, Luisa Eck, Peter Vincent Gehler, Oliver Bringmann, Wieland Brendel, and Matthias Bethge. 2022. [If your data distribution shifts, use self-learning](#). *Transactions on Machine Learning Research*. Expert Certification.

Kuniaki Saito, Donghyun Kim, Stan Sclaroff, Trevor Darrell, and Kate Saenko. 2019. Semi-supervised domain adaptation via minimax entropy. In *Proceedings of the IEEE/CVF international conference on computer vision*, pages 8050–8058.

Jian Shen, Yanru Qu, Weinan Zhang, and Yong Yu. 2018. Wasserstein distance guided representation learning for domain adaptation. In *Proceedings of the AAAI conference on artificial intelligence*, volume 32.

Manli Shu, Weili Nie, De-An Huang, Zhiding Yu, Tom Goldstein, Anima Anandkumar, and Chaowei Xiao. 2022. Test-time prompt tuning for zero-shot generalization in vision-language models. *Advances in Neural Information Processing Systems*, 35:14274–14289.

Baochen Sun, Jiashi Feng, and Kate Saenko. 2017. Correlation alignment for unsupervised domain adaptation. In *Domain adaptation in computer vision applications*, pages 153–171. Springer.

Baochen Sun and Kate Saenko. 2016. Deep coral: Correlation alignment for deep domain adaptation. In *European conference on computer vision*, pages 443–450. Springer.

Hugo Touvron, Thibaut Lavril, Gautier Izacard, Xavier Martinet, Marie-Anne Lachaux, Timothée Lacroix, Baptiste Rozière, Naman Goyal, Eric Hambro, Faisal Azhar, and 1 others. 2023. Llama: Open and efficient foundation language models. *arXiv preprint arXiv:2302.13971*.

Boxin Wang, Weixin Chen, Hengzhi Pei, Chulin Xie, Mintong Kang, Chenhui Zhang, Chejian Xu, Zidi Xiong, Ritik Dutta, Rylan Schaeffer, and 1 others. 2023a. Decodingtrust: A comprehensive assessment of trustworthiness in gpt models. In *NeurIPS*.

Dequan Wang, Evan Shelhamer, Shaoteng Liu, Bruno Olshausen, and Trevor Darrell. 2020. Tent: Fully test-time adaptation by entropy minimization. *arXiv preprint arXiv:2006.10726*.

Dingsu Wang, Yuchen Yan, Ruizhong Qiu, Yada Zhu, Kaiyu Guan, Andrew Morgenot, and Hanghang Tong. 2023b. Networked time series imputation via position-aware graph enhanced variational autoencoders. In *Proceedings of the 29th ACM SIGKDD Conference on Knowledge Discovery and Data Mining*, pages 2256–2268.

Ruijie Wang, Baoyu Li, Yichen Lu, Dachun Sun, Jining Li, Yuchen Yan, Shengzhong Liu, Hanghang Tong, and Tarek F Abdelzaher. 2023c. Noisy positive-unlabeled learning with self-training for speculative knowledge graph reasoning. *arXiv preprint arXiv:2306.07512*.

Ruijie Wang, Yuchen Yan, Jialu Wang, Yuting Jia, Ye Zhang, Weinan Zhang, and Xinbing Wang. 2018. Acekg: A large-scale knowledge graph for academic data mining. In *Proceedings of the 27th ACM international conference on information and knowledge management*, pages 1487–1490.

Xu Wang, Dezhong Peng, Ming Yan, and Peng Hu. 2023d. Correspondence-free domain alignment for unsupervised cross-domain image retrieval. In *Proceedings of the AAAI Conference on Artificial Intelligence*, volume 37, pages 10200–10208.

Haobo Xu, Yuchen Yan, Dingsu Wang, Zhe Xu, Zhichen Zeng, Tarek F Abdelzaher, Jiawei Han, and Hanghang Tong. Slog: An inductive spectral graph neural network beyond polynomial filter. In *Forty-first International Conference on Machine Learning*.

Minghao Xu, Hang Wang, Bingbing Ni, Qi Tian, and Wenjun Zhang. 2020. Cross-domain detection via graph-induced prototype alignment. In *Proceedings of the IEEE/CVF conference on computer vision and pattern recognition*, pages 12355–12364.

Hongliang Yan, Yukang Ding, Peihua Li, Qilong Wang, Yong Xu, and Wangmeng Zuo. 2017. Mind the class weight bias: Weighted maximum mean discrepancy for unsupervised domain adaptation. In *Proceedings of the IEEE conference on computer vision and pattern recognition*, pages 2272–2281.

Yuchen Yan, Yuzhong Chen, Huiyuan Chen, Xiaoting Li, Zhe Xu, Zhichen Zeng, Lihui Liu, Zhining Liu, and Hanghang Tong. 2024a. Thegcn: Temporal heterophilic graph convolutional network. *arXiv preprint arXiv:2412.16435*.

Yuchen Yan, Yuzhong Chen, Huiyuan Chen, Minghua Xu, Mahashweta Das, Hao Yang, and Hanghang Tong. 2023a. From trainable negative depth to edge heterophily in graphs. *Advances in Neural Information Processing Systems*, 36:70162–70178.

Yuchen Yan, Yongyi Hu, Qinghai Zhou, Lihui Liu, Zhichen Zeng, Yuzhong Chen, Menghai Pan, Huiyuan Chen, Mahashweta Das, and Hanghang Tong. 2024b. Pacer: Network embedding from positional to structural. In *Proceedings of the ACM Web Conference 2024*, pages 2485–2496.

Yuchen Yan, Yongyi Hu, Qinghai Zhou, Shurang Wu, Dingsu Wang, and Hanghang Tong. 2024c. Topological anonymous walk embedding: A new structural node embedding approach. In *Proceedings of the 33rd ACM International Conference on Information and Knowledge Management*, pages 2796–2806.

Yuchen Yan, Baoyu Jing, Lihui Liu, Ruijie Wang, Jining Li, Tarek Abdelzaher, and Hanghang Tong. 2023b. Reconciling competing sampling strategies of network embedding. *Advances in Neural Information Processing Systems*, 36:6844–6861.

Yuchen Yan, Aakash Kolekar, Sahika Genc, Wenju Xu, Edward W Huang, Anirudh Srinivasan, Mukesh Jain, Qi He, and Hanghang Tong. 2025. To answer or not to answer (taona): A robust textual graph understanding and question answering approach. In *Findings of the Association for Computational Linguistics: EMNLP 2025*, pages 6360–6376.

Yuchen Yan, Lihui Liu, Yikun Ban, Baoyu Jing, and Hanghang Tong. 2021a. Dynamic knowledge graph alignment. In *Proceedings of the AAAI conference on artificial intelligence*, volume 35, pages 4564–4572.

Yuchen Yan, Si Zhang, and Hanghang Tong. 2021b. Bright: A bridging algorithm for network alignment. In *Proceedings of the web conference 2021*, pages 3907–3917.

Yuchen Yan, Qinghai Zhou, Jining Li, Tarek Abdelzaher, and Hanghang Tong. 2022. Dissecting cross-layer dependency inference on multi-layered interdependent networks. In *Proceedings of the 31st ACM International Conference on Information & Knowledge Management*, pages 2341–2351.

Xiaodong Yang, Huiyuan Chen, Yuchen Yan, Yuxin Tang, Yuying Zhao, Eric Xu, Yiwei Cai, and Hanghang Tong. 2024. Simce: Simplifying cross-entropy loss for collaborative filtering. *arXiv preprint arXiv:2406.16170*.

Hyunsik Yoo, Zhichen Zeng, Jian Kang, Ruizhong Qiu, David Zhou, Zhining Liu, Fei Wang, Charlie Xu, Eunice Chan, and Hanghang Tong. 2024. Ensuring user-side fairness in dynamic recommender systems. In *Proceedings of the ACM Web Conference 2024*, pages 3667–3678.

Jiahui Yu, Zirui Wang, Vijay Vasudevan, Legg Yehung, Mojtaba Seyedhosseini, and Yonghui Wu. 2022. Coca: Contrastive captioners are image-text foundation models. *arXiv preprint arXiv:2205.01917*.

Qi Yu, Zhichen Zeng, Yuchen Yan, Zhining Liu, Baoyu Jing, Ruizhong Qiu, Ariful Azad, and Hanghang Tong. 2025a. Planetalign: A comprehensive python library for benchmarking network alignment. *arXiv preprint arXiv:2505.21366*.

Qi Yu, Zhichen Zeng, Yuchen Yan, Lei Ying, R Srikant, and Hanghang Tong. 2025b. Joint optimal transport and embedding for network alignment. In *Proceedings of the ACM on Web Conference 2025*, pages 2064–2075.

Shoubin Yu, Jaemin Cho, Prateek Yadav, and Mohit Bansal. 2023. Self-chained image-language model for video localization and question answering. *Advances in Neural Information Processing Systems*, 36:76749–76771.

Longhui Yuan, Binhui Xie, and Shuang Li. 2023. Robust test-time adaptation in dynamic scenarios. In *Proceedings of the IEEE/CVF Conference on Computer Vision and Pattern Recognition*, pages 15922–15932.

Zhichen Zeng, Boxin Du, Si Zhang, Yinglong Xia, Zhining Liu, and Hanghang Tong. 2024a. Hierarchical multi-marginal optimal transport for network alignment. In *Proceedings of the AAAI Conference on Artificial Intelligence*, volume 38, pages 16660–16668.

Zhichen Zeng, Mengyue Hang, Xiaolong Liu, Xiaoyi Liu, Xiao Lin, Ruizhong Qiu, Tianxin Wei, Zhining Liu, Siyang Yuan, Chaofei Yang, and 1 others. 2025a. Hierarchical lora moe for efficient ctr model scaling. *arXiv preprint arXiv:2510.10432*.

Zhichen Zeng, Xiaolong Liu, Mengyue Hang, Xiaoyi Liu, Qinghai Zhou, Chaofei Yang, Yiqun Liu, Yichen Ruan, Laming Chen, Yuxin Chen, and 1 others. 2025b. Interformer: Effective heterogeneous interaction learning for click-through rate prediction. In *Proceedings of the 34th ACM International Conference on Information and Knowledge Management*, pages 6225–6233.

Zhichen Zeng, Ruizhong Qiu, Wenxuan Bao, Tianxin Wei, Xiao Lin, Yuchen Yan, Tarek F Abdelzaher, Jiawei Han, and Hanghang Tong. 2025c. Pave your own path: Graph gradual domain adaptation on fused gromov-wasserstein geodesics. *arXiv preprint arXiv:2505.12709*.

Zhichen Zeng, Ruizhong Qiu, Zhe Xu, Zhining Liu, Yuchen Yan, Tianxin Wei, Lei Ying, Jingrui He, and Hanghang Tong. 2024b. Graph mixup on approximate gromov-wasserstein geodesics. In *Forty-first International Conference on Machine Learning*.

Zhichen Zeng, Qi Yu, Xiao Lin, Ruizhong Qiu, Xuying Ning, Tianxin Wei, Yuchen Yan, Jingrui He, and Hanghang Tong. 2025d. Harnessing consistency for robust test-time llm ensemble. *arXiv preprint arXiv:2510.13855*.

Zhichen Zeng, Si Zhang, Yinglong Xia, and Hanghang Tong. 2023a. Parrot: Position-aware regularized optimal transport for network alignment. In *Proceedings of the ACM web conference 2023*, pages 372–382.

Zhichen Zeng, Ruike Zhu, Yinglong Xia, Hanqing Zeng, and Hanghang Tong. 2023b. Generative graph dictionary learning. In *International Conference on Machine Learning*, pages 40749–40769. PMLR.

Marvin Zhang, Sergey Levine, and Chelsea Finn. 2022. Memo: Test time robustness via adaptation and augmentation. *Advances in neural information processing systems*, 35:38629–38642.

Yabin Zhang, Wenjie Zhu, Hui Tang, Zhiyuan Ma, Kaiyang Zhou, and Lei Zhang. 2024. Dual memory networks: A versatile adaptation approach for vision-language models. In *Proceedings of the IEEE/CVF conference on computer vision and pattern recognition*, pages 28718–28728.

Yuheng Zhang, Dian Yu, Tao Ge, Linfeng Song, Zhichen Zeng, Haitao Mi, Nan Jiang, and Dong Yu. 2025. Improving llm general preference alignment via optimistic online mirror descent. *arXiv preprint arXiv:2502.16852*.

Chuang Zhao, Hongke Zhao, Ming He, Jian Zhang, and Jianping Fan. 2023a. Cross-domain recommendation via user interest alignment. In *Proceedings of the ACM web conference 2023*, pages 887–896.

Chuang Zhao, Hongke Zhao, Xiaomeng Li, Ming He, Jiahui Wang, and Jianping Fan. 2023b. Cross-domain recommendation via progressive structural alignment. *IEEE Transactions on Knowledge and Data Engineering*, 36(6):2401–2415.

Xinge Zhu, Jiangmiao Pang, Ceyuan Yang, Jianping Shi, and Dahua Lin. 2019. Adapting object detectors via selective cross-domain alignment. In *Proceedings of the IEEE/CVF conference on computer vision and pattern recognition*, pages 687–696.

Xingyu Zhu, Beier Zhu, Yi Tan, Shuo Wang, Yanbin Hao, and Hanwang Zhang. 2024. Selective vision-language subspace projection for few-shot clip. In *ACM Multimedia 2024*.

## Appendix

### A Experiments

#### A.1 Experiment Pipeline

Following the established TTA protocol (Wang et al., 2020), we conduct experiments under the highest severity level (Level 5) to simulate severe distribution shifts. We adopt an online adaptation setting where the model adapts to a continuous stream of unlabeled test data for each corruption type independently, resetting the model state between corruptions. All experiments are executed on NVIDIA A100 80GB GPUs.

#### A.2 Additional Results

##### A.2.1 Results with Different Backbones

To verify the scalability and generalization of our approach, we provide detailed benchmark results using ViT-B-32 and ViT-L-14 backbones in Table 2 and Table 3, respectively. The results align with the observations on ViT-B-16 reported in the main text, confirming three key trends:

**(1) Consistent SOTA performance across model capacities.** SubTTA maintains its superiority regardless of the backbone architecture. On the lower-capacity ViT-B-32, SubTTA achieves a mean accuracy of 30.50% on ImageNet-C, outperforming the runner-up BATCLIP (27.37%) by a substantial margin of 3.13%. On the stronger ViT-L-14, SubTTA continues to set the state-of-the-art with 44.55% mean accuracy. This confirms that our geometric rectification is effective for both rescuing weaker models and refining stronger ones.

**(2) Elimination of negative adaptation.** Similar to the ViT-B-16 settings, baseline methods exhibit instability under heavy noise. For instance, on ViT-B-32, TENT suffers from negative adaptation on Gaussian Noise (12.16% vs. Source 12.90%). In contrast, SubTTA consistently improves over the source baseline across all corruption categories for both backbones, demonstrating robust stability against severe distribution shifts.

**(3) Validation of the paradigm hierarchy.** The performance hierarchy observed in the main text holds true across different backbones: training-based methods generally outperform training-free ones, and cluster-based objectives (e.g., MINT, BATCLIP) consistently surpass entropy-based approaches (e.g., TENT). SubTTA builds upon the robust cluster-based paradigm and further elevates

it via subspace alignment, yielding the most reliable adaptation performance.

### B Algorithm

We provide the pseudo code of SubTTA in Algorithm 1, which includes three steps: geometric alignment, semantic projection and standard TTA.

---

#### Algorithm 1 SubTTA

---

**Input:** Image encoder  $f_v$ ; text encoder  $f_t$ ; image batches  $\mathcal{D}_{\text{test}} = \{\mathbf{X}^{(1)}, \mathbf{X}^{(2)}, \dots\}$ ; textual prompts  $t_1, \dots, t_C$ ; subspace rank  $r$ ; momentum coefficient  $\alpha$ .

**Output:** Prediction  $\hat{Y}$  for the test images.

*Stage 1: Textual Subspace Initialization*

- 1: Extract normalized text features  $\mathbf{T} = [\mathbf{t}_1, \dots, \mathbf{t}_C]^T \in \mathbb{R}^{C \times d}$  with  $\mathbf{t}_i = f_t(t_i)$ .
- 2: Compute textual covariance  $\Sigma_{\mathcal{T}} = \mathbf{T}^T \mathbf{T}$ .
- 3: Compute textual basis  $\mathbf{B}_{\mathcal{T}} \in \mathbb{R}^{r \times d}$  via Eq. (2).
- 4: Initialize visual covariance prior  $\Sigma_{\mathcal{V}} \leftarrow \Sigma_{\mathcal{T}}$ .

*Stage 2: Online Test-Time Adaptation*

- 5: **for** each test batch  $\mathbf{X}^{(k)}$  in  $\mathcal{D}_{\text{test}}$  **do**
- 6:   Extract visual features  $\mathbf{V}^{(k)} = f_v(\mathbf{X}^{(k)}) \in \mathbb{R}^{B \times d}$ .
- 7:   Visual covariance EMA via Eq. (1)
- 8:   Compute visual basis  $\mathbf{B}_{\mathcal{V}} \in \mathbb{R}^{r \times d}$  via Eq. (2).
- 9:   **Step 1: Geometric Alignment**
- 10:   Compute alignment loss  $\mathcal{L}_{\text{align}}$  in Eq. (4).
- 11:   Update model parameters  $\theta$  by Adam with  $\nabla_{\theta} \mathcal{L}_{\text{align}}$ .
- 12:   **Step 2: Semantic Projection**
- 13:   Extract image features  $\tilde{\mathbf{V}}^{(k)}$  using updated model.
- 14:   Project features onto textual subspace via Eq. (3.3)
- 15:   **Step 3: Standard TTA**
- 16:   Compute standard TTA loss  $\mathcal{L}_{\text{TTA}}$  (e.g., MINT or Entropy) on purified features  $\mathbf{V}_{\text{proj}}$ .
- 17:   Update model parameters  $\theta$  by Adam with  $\nabla_{\theta} \mathcal{L}_{\text{TTA}}$ .
- 18:   Compute prediction  $\hat{Y}^{(k)} = \arg \max_c \mathbf{V}_{\text{proj}} \mathbf{T}^T$ .
- 19:   **end for**
- 20: **return** TTA predictions  $\hat{Y}^{(1)}, \hat{Y}^{(2)}, \dots$

---

### C Datasets

We introduce the datasets adopted in this work.

**ImageNet-C** (Hendrycks and Dietterich, 2019) is a robustness benchmark derived from ImageNet. It spans 1,000 object classes and contains 50,000 test images for each corruption type and severity level. **CIFAR-10-C** (Hendrycks and Dietterich, 2019) is constructed from the CIFAR-10. It comprises 10,000 images distributed across 10 distinct classes. **CIFAR-100-C** (Hendrycks and Dietterich, 2019) is an extension of the CIFAR-100, containing 10,000 images covering 100 fine-grained classes.

All three datasets employ a shared set of 15 algorithmically generated corruptions to assess model robustness under distribution shifts. These corruptions are categorized into four primary groups: noise, blur, weather, and digital distortions, and

Table 2: Benchmark results with ViT-B-32. We denote Top-1/2/3 by Blue/Yellow/red, respectively.

Method	Noise			Blur			Weather				Digital			Mean			
	Gauss.	Shot	Impul.	Defoc.	Glass	Motion	Zoom	Snow	Frost	Fog	Brit.	Contr.	Elast.	Pixel.	JPEG		
ImageNet-C	Source	12.90	13.06	12.80	24.38	11.82	22.68	20.24	25.60	25.84	30.24	50.48	17.30	18.98	32.32	29.10	23.18
	TDA	12.80	14.72	14.84	24.14	12.98	23.46	20.98	26.74	28.00	32.28	51.64	18.16	20.70	33.00	30.20	24.31
	DMN	13.00	14.32	14.50	22.92	11.78	22.18	19.68	23.70	25.72	29.62	50.50	14.78	19.92	32.46	29.36	22.96
	VTE	11.98	12.32	13.44	25.06	11.60	22.60	22.34	27.40	27.04	32.28	51.62	16.82	20.02	34.80	32.78	24.14
	ZERO	12.36	12.88	12.58	24.90	12.06	22.84	21.46	26.72	26.64	30.58	50.98	16.80	19.66	33.82	30.52	23.65
	ECALP	14.40	15.10	14.68	23.28	12.18	23.18	21.08	24.40	25.38	29.50	47.92	18.26	19.12	31.42	29.00	23.26
	RoTTA	13.22	13.30	13.10	24.52	12.02	22.93	20.30	25.88	26.00	30.34	50.46	17.40	19.10	32.38	29.22	23.34
	TPT	12.16	12.60	12.48	25.36	12.22	22.42	20.94	26.70	26.78	30.50	50.82	16.88	19.88	33.40	30.50	23.58
	MEMO	12.84	13.00	12.78	24.66	11.88	22.82	20.40	25.70	26.00	30.28	50.50	17.32	19.02	32.48	29.14	23.25
	WATT	14.28	14.64	14.42	25.62	15.26	25.52	21.92	26.76	25.86	31.44	50.70	22.22	19.68	33.56	30.64	24.83
BATCLIP	MINT	18.84	19.98	19.42	24.86	19.08	27.20	22.44	27.94	27.28	32.72	50.64	20.18	24.04	34.84	33.14	26.84
	SubTTA	17.64	18.60	16.98	24.56	20.40	28.46	24.66	29.16	27.02	35.76	49.56	20.56	27.62	35.24	34.26	27.37
		22.56	23.52	23.02	25.66	23.36	28.46	27.42	31.18	32.32	39.08	50.50	26.00	33.00	37.12	34.28	30.50
CIFAR10-C	Source	35.51	40.01	43.17	69.91	41.46	64.52	70.10	70.84	72.32	66.65	81.35	64.48	59.69	48.18	56.62	58.99
	TDA	41.49	43.44	41.44	71.14	44.86	66.96	72.37	72.20	74.53	68.46	83.57	65.64	62.61	51.14	55.67	61.03
	DMN	38.83	39.45	42.12	70.74	39.48	65.01	72.78	72.52	73.41	66.45	82.39	58.46	60.51	49.05	55.92	59.14
	VTE	47.55	50.18	53.11	71.35	53.87	67.89	72.95	76.37	76.24	70.76	83.33	61.05	68.99	58.57	61.07	64.89
	ZERO	37.11	41.66	46.79	71.21	42.51	65.21	71.58	72.27	73.79	68.92	82.78	65.53	62.35	47.66	58.80	60.54
	ECALP	44.36	47.05	43.93	71.17	43.56	68.32	73.92	72.49	74.92	68.06	82.61	62.95	61.91	47.18	55.67	61.21
	RoTTA	36.36	41.12	43.76	69.94	42.44	64.68	70.06	71.34	72.83	67.33	81.74	65.12	60.41	49.37	57.26	59.58
	TPT	43.13	46.67	48.30	71.33	47.77	66.95	72.05	73.95	76.09	68.73	84.16	66.31	63.91	51.82	58.02	62.61
	MEMO	36.50	40.68	44.28	70.81	42.10	64.67	70.63	72.17	73.01	67.63	82.10	64.25	61.03	47.84	57.61	59.69
	WATT	43.63	48.69	49.13	72.23	46.15	66.74	71.04	73.64	74.46	71.25	83.99	73.12	61.98	59.25	62.98	63.89
CIFAR100-C	MINT	54.18	57.78	47.30	73.49	56.01	73.71	76.39	74.94	74.46	70.16	85.66	70.60	64.66	58.85	59.53	66.51
	BATCLIP	52.19	55.70	53.96	76.09	55.09	74.75	75.18	77.23	78.09	74.97	86.03	77.37	67.53	58.01	61.90	68.27
	SubTTA	60.43	63.78	56.40	78.48	61.66	76.24	77.26	80.03	79.99	77.95	88.72	83.62	70.51	73.77	63.46	72.82

each is applied at five severity levels. The *noise* category includes Gaussian, shot, and impulse noise, which introduce random pixel-level variations. The *blur* category encompasses defocus, glass, motion, and zoom blur, simulating various optical distortions. *Weather*-related corruptions, such as snow, frost, and fog, replicate environmental conditions that obscure image details. Lastly, *digital* distortions include brightness, contrast, elastic transform, pixelate, and JPEG compression, reflecting common post-processing or compression artifacts.

## D More Related Works

We provide more related works on pre-trained foundation models, domain adaptation and cross-domain alignment.

**Pre-trained Foundation Models.** Foundation models have reshaped the field by pretraining models on vast amounts of web-scale data (Achiam et al., 2023; Touvron et al., 2023; Lin et al., 2025a, 2024a; Li et al., 2025c; Ai et al., 2025; Cui et al., 2026). Large Language Models (LLMs) have demonstrated remarkable generalization capabil-

ities with various applications in natural language understanding (Achiam et al., 2023; Touvron et al., 2023; Zhang et al., 2025), numerical analysis (Li et al., 2025b; Jing et al.), and ethics evaluation (Lin et al., 2025b). Parallel to this success, encoder-decoder VLMs such as CLIP (Radford et al., 2021) and ALIGN (Jia et al., 2021) extend this paradigm to the visual domain by aligning images and text in a shared embedding space via contrastive learning. This joint training enables powerful zero-shot transfer to downstream tasks without task-specific fine-tuning. Decoder-only VLMs like Flamingo (Alayrac et al., 2022), BLIP-2 (Li et al., 2023), and LLaVA (Liu et al., 2023) leverage visual instruction tuning to project visual features into the input space of frozen LLMs, unlocking capabilities for complex multimodal understanding and dialogue. Despite their impressive capabilities, these models remain vulnerable to distribution shifts when deployed in open-world environments, and significant efforts have been made on improving the robustness of LLMs and VLMs (Qi et al., 2024; Wang et al., 2023a; Yan et al., 2025; Lin

Table 3: Benchmark results with ViT-L-14. We denote Top-1/2/3 by Blue/Yellow/red, respectively.

Method	Noise			Blur			Weather				Digital			Mean			
	Gauss.	Shot	Impul.	Defoc.	Glass	Motion	Zoom	Snow	Frost	Fog	Brit.	Contr.	Elast.	Pixel.	JPEG		
ImageNet-C	Source	27.40	29.42	28.72	34.58	25.28	40.96	36.70	49.80	44.10	49.78	65.36	35.18	30.42	53.48	42.24	39.56
	TDA	27.52	30.72	32.30	35.20	27.04	42.60	38.20	51.40	46.36	52.08	66.76	37.70	31.76	55.22	44.00	41.26
	DMN	27.44	30.16	30.84	32.72	25.98	41.26	37.00	49.54	44.56	50.02	66.00	29.50	31.10	54.90	42.18	39.55
	VTE	26.36	29.20	28.98	36.38	24.88	40.92	39.36	50.52	44.92	50.86	67.42	33.80	30.56	55.58	47.76	40.50
	ZERO	27.12	28.70	28.72	35.54	25.66	40.50	38.16	50.56	43.84	50.32	66.04	35.24	30.74	55.08	44.98	40.08
	ECALP	29.48	30.34	30.86	35.60	27.50	42.82	38.38	50.48	45.42	50.52	65.40	37.44	30.12	55.16	42.80	40.82
	RoTTA	27.62	29.60	29.02	34.68	25.50	41.18	36.82	50.04	44.20	49.76	65.40	35.08	30.82	53.64	42.36	39.71
	TPT	27.08	30.00	29.54	35.84	25.78	41.50	37.98	51.64	45.72	51.78	67.78	36.34	31.64	55.56	46.16	40.96
	MEMO	27.42	29.46	28.74	34.66	25.34	41.00	36.74	49.78	44.16	49.80	65.42	35.16	30.40	53.56	42.24	39.59
	WATT	29.82	31.42	30.70	36.68	28.92	42.30	38.48	51.10	44.46	50.70	65.60	39.18	33.54	54.16	43.30	41.36
CIFAR10-C	MINT	32.00	33.20	33.84	37.22	33.38	43.68	39.28	53.62	45.62	53.42	66.34	39.16	37.32	55.46	49.22	43.52
	BATCLIP	31.44	31.40	30.94	35.84	31.68	43.72	39.26	50.16	43.02	51.12	65.50	40.14	35.38	53.68	48.92	42.15
	SubTTA	32.96	35.28	36.48	35.70	34.86	44.02	41.34	53.22	47.12	55.70	65.74	46.30	35.88	55.82	47.84	44.55
	Source	64.33	67.10	75.90	80.47	51.55	80.34	83.04	83.21	84.92	79.14	91.07	84.09	66.44	73.60	72.26	75.83
	TDA	68.32	70.62	75.97	80.67	50.18	81.03	83.07	84.32	85.82	79.02	91.78	84.65	66.94	73.93	73.70	76.67
	DMN	68.64	69.94	74.76	76.33	51.12	79.33	80.86	84.94	85.87	79.15	91.94	84.57	66.20	71.97	73.34	75.93
	VTE	63.90	66.97	75.24	78.72	51.65	79.43	81.32	83.60	85.27	76.43	90.13	81.33	70.11	74.85	70.79	75.32
	ZERO	66.12	69.49	76.85	81.97	53.45	80.71	84.40	85.19	86.59	79.83	92.19	84.51	69.94	74.40	73.71	77.29
	ECALP	70.41	72.13	79.90	80.93	54.42	81.07	83.70	84.92	86.51	79.44	92.25	84.69	68.12	74.67	73.61	77.78
	RoTTA	65.73	68.49	76.57	80.54	52.39	80.51	83.29	83.56	85.35	79.51	91.28	84.30	67.01	74.62	73.07	76.41
	TPT	67.15	69.87	79.01	80.83	55.33	81.17	83.43	85.14	86.97	79.81	92.16	83.87	70.87	76.52	74.07	77.75
CIFAR100-C	MEMO	64.88	67.74	76.40	80.83	52.16	80.58	83.46	83.84	85.51	79.40	91.38	84.11	67.45	73.90	73.20	76.32
	WATT	70.84	72.44	77.03	82.83	61.91	82.35	85.15	85.70	86.98	81.93	91.84	88.25	72.04	77.76	77.15	79.61
	MINT	68.12	73.40	77.52	85.58	63.27	83.93	87.00	86.77	88.39	83.15	94.12	88.96	73.42	79.10	76.07	80.59
	BATCLIP	74.81	78.11	83.70	87.53	71.62	86.74	89.29	89.99	89.73	87.53	94.65	92.29	78.92	83.37	80.09	84.56
	SubTTA	77.28	79.97	84.14	87.67	70.00	86.87	88.82	88.95	89.87	88.28	93.81	93.37	78.42	83.86	78.90	84.68

et al., 2026; Zeng et al., 2025d), necessitating effective adaptation strategies to bridge the gap between pre-training and testing stages.

**Domain Adaptation.** The challenge of generalizing models to out-of-distribution data has evolved through increasingly constrained settings, spanning from label-scarce scenarios to fully unsupervised and source-free environments.

(*Semi-)supervised domain adaptation (SSDA)* represents the most accessible settings, assuming the availability of at least a few labeled samples in the target domain (Motian et al., 2017; Saito et al., 2019). Approaches typically leverage the limited target labels to perform fine-tuning or align class-conditional distributions via metric learning (Kang et al., 2019) and minimax entropy training (Saito et al., 2019). However, the reliance on target annotation, even if minimal, limits their scalability in open-world deployments.

*Unsupervised Domain Adaptation (UDA)* removes the reliance on target labels, assuming access to both labeled source data and fully unlabeled target data. Methods in this realm can be broadly

categorized into two streams. One prominent line of works employ adversarial learning (Ganin and Lempitsky, 2015), optimizing a domain discriminator to force the feature extractor to learn domain-invariant representations. Another line of works minimize the discrepancy between source and target distributions such as maximum mean discrepancy (Long et al., 2015; Yan et al., 2017), Wasserstein distance (Shen et al., 2018; Zeng et al., 2025c) and correlation alignment (Sun and Saenko, 2016; Sun et al., 2017; Lin et al., 2025c).

*Test-time adaptation (TTA)* faces the most challenging setting, imposing strict latency and online constraints where data arrives in streams (Wang et al., 2020). Existing TTA strategies generally diverge into three optimization categories: First (entropy minimization (Wang et al., 2020; Zhang et al., 2022)), which sharpens prediction distributions to reduce uncertainty; Second (self-training with pseudo-labels (Rusak et al., 2022; Bao et al., 2025, 2024; Yang et al., 2024)), which utilizes robust loss functions or cluster structures to refine decision boundaries. Third (parameter-efficient tuning (Shu et al., 2022)), which updates only specific

modules (e.g., prompts or normalization layers) to prevent catastrophic forgetting.

**Cross-Domain Alignment.** To mitigate the discrepancy between domains, various alignment strategies (Yan et al., 2021a,b, 2022; Zeng et al., 2023a, 2024a; Yu et al., 2025b,a) have been proposed to learn domain-invariant representations (Du et al., 2021; Roach et al., 2020; Wang et al., 2018, 2023b,c), with applications in various data modalities such as image (Zhu et al., 2019; Xu et al., 2020; Wang et al., 2023d), text (Liu et al., 2021; Chen et al., 2020), graphs (Yan et al., 2023a,b, 2024b,c,a; Xu et al.; Zeng et al., 2023b, 2024b; Lin et al., 2024b,c), time series (Lin et al., 2024d; Qiu et al., 2025; Liu et al., 2025) and recommendation (Zhao et al., 2023a,b; Zeng et al., 2025b,a; Yoo et al., 2024; Liu et al., 2024; Liang et al., 2025). One prevalent approach is *statistical moment matching*, which explicitly minimizes the distance between feature distributions (Long et al., 2015; Sun and Saenko, 2016). Another significant direction is *manifold alignment*, which posits that domain shifts can be modeled as geometric transformations (Fernando et al., 2013; Gong et al., 2012). While these classical methods laid the theoretical groundwork, they typically require offline processing or access to source data. SubTTA revitalizes these geometric principles, adapting the manifold alignment concept to the challenging online, source-free TTA setting by utilizing the textual subspace as a stable semantic anchor. Beyond image–text alignment, several pioneering studies further extend alignment paradigms to graph (Li et al., 2025e) and time-series domains (Li et al., 2025d), which inspire some future directions of SubTTA.

## E Dataset Statistics

Dataset statistics are summarized as follows based on the details in Appendix C.

### E.1 ImageNet-C

- Number of classes: 1,000 object classes.
- Size: 50,000 test images for each corruption type and severity level.
- Structure: Derived from ImageNet validation set with 15 algorithmically generated corruptions.

### E.2 CIFAR-10-C

- Number of classes: 10 distinct classes.
- Size: 10,000 test images.
- Structure: Derived from CIFAR-10 test set with 15 algorithmically generated corruptions.

### E.3 CIFAR-100-C

- Number of classes: 100 fine-grained classes.
- Size: 10,000 test images.
- Structure: Derived from CIFAR-100 test set with 15 algorithmically generated corruptions.

## F Computational Experiments

All computational experiments in this work are fully reproducible, with details provided in Section 4.1 and Appendix A.1.

### F.1 Model Size And Budget

We evaluate our method on CLIP models with varying capacities, including:

- ViT-B-16: 112M total parameters, and 41k trainable parameters.
- ViT-B-32: 113M total parameters, and 41k trainable parameters.
- ViT-L-14: 343M total parameters, and 104k trainable parameters.

All experiments are executed on NVIDIA A100 80GB GPUs.

### F.2 Experimental Setup And Hyper-params

We describe experimental settings in Section 4.1. We adopt an online adaptation setting where the model adapts to a continuous stream of unlabeled test data for each corruption type independently (resetting between corruptions). Key hyperparameters studied in Section 4.5.2 include:

- Subspace rank  $r$ : We vary  $r$  (e.g., 64, 128, 256) and find that avoiding extremes (too compressed or full-rank) is optimal.
- Momentum coefficient  $\alpha$ : We use an EMA strategy for covariance updates, with stability observed for  $\alpha \in (0.2, 0.8)$ .
- Batch Size: We investigate the impact of batch size, and results indicate that larger batch sizes (e.g., 64 and above) provide stable covariance estimation and consistent performance, whereas smaller batches (e.g., 16) may lead to instability.